Particle-induced miscible fingering: Continuum limit

Rui Luo, Yun Chen, and Sungyon Lee*
Department of Mechanical Engineering, University of Minnesota, Minneapolis, Minnesota 55455, USA

(Received 2 May 2020; accepted 12 August 2020; published 11 September 2020)

We experimentally inject silicone oil into the mixture of oil and noncolloidal particles inside a Hele-Shaw cell, to investigate the connection between miscible fingering and the interfacial structure that develops inside the thin gap. Previous studies with pure fluids have demonstrated that the onset of miscible fingering coincides with the transition from a smooth tonguelike structure to a sharp front between invading and defending fluids inside the gap. Our current experiments with suspensions reveal the same general behavior at the onset of miscible fingering, which we capture qualitatively using a lubrication model. However, distinct from the pure liquid counterpart, we observe changes in the interfacial structures inside the gap as the ratio of the gap thickness to particle diameter is systematically varied. We demonstrate that the particle dynamics inside the thin gap may alter interfacial structures even within the continuum limit, which lead to changes in morphologies of miscible fingering. The results of our study suggest a potential use of the wall confinement to control hydrodynamic instabilities in suspensions.

DOI: 10.1103/PhysRevFluids.5.094301

I. INTRODUCTION

Viscous fingering occurs when a less viscous fluid displaces a more viscous one inside porous media [1,2]. This hydrodynamic instability has been thoroughly studied both experimentally and theoretically, due to its relevance in hydrology and various oil recovery processes [3]. For viscous fingering between two immiscible fluids inside a Hele-Shaw cell, Saffman and Taylor derived the most unstable wavelength λ_c [1], which is governed by the competition between surface tension and viscous forces. Following this seminal work in Ref. [1], extensive theoretical investigations have been made based on Darcy's law, to successfully describe immiscible viscous fingering [4–8].

In the absence of surface tension, the critical wavelength based on Darcy's law tends to zero, which has been shown to break down in the experiments [9,10]. Wooding [9] experimentally observed finite fingers between miscible fluids at high Péclet numbers, that are comparable to those between immiscible fluids inside a Hele-Shaw cell. Fingers with finite wavelengths were again observed by Paterson [10] who experimentally tested the penetration of water into glycerol inside a Hele-Shaw cell. To rationalize the emergence of finite fingers even without surface tension, Paterson developed a theoretical model that assumes a three-layer structure (e.g., a plug flow) within the gap, in lieu of Darcy's law, and correctly predicted the most unstable wavelength. Recent theoretical studies [11,12] demonstrated the selection of finite wavelengths in the limit of zero surface tension, by implementing viscous stresses at the interface in a depth-averaged model.

In addition to finite wavelengths, another unexpected feature of miscible displacements at high Péclet numbers is a suppression of viscous fingering at finite viscosity ratios. Lajeunesse *et al.* [13,14] experimentally identified the minimum viscosity ratio necessary for miscible viscous fingering. They also developed a theoretical model of interfacial structures inside the gap, by

*sungyon@umn.edu

extending the lubrication model by Yang and Yortsos [15] for miscible displacements at high Péclet numbers. Their theoretical results demonstrated that the onset of miscible fingering is directly tied to the transition in interfacial structures from being smooth to forming shock fronts. Then, Oliveira and Meiburg [16] conducted 3D simulations of miscible displacements within pure fluids and predicted an inner-splitting phenomenon. Their numerical investigation verified the inherent three-dimensional nature of miscible fingering at a high Péclet number, which cannot be captured with depth-averaged flow equations.

More recently, Bischofberger *et al.* [17] conducted systematic experiments analyzing the global feature of miscible fingering within pure fluids inside a radial Hele-Shaw cell. Consistent with the work of Lajeunesse *et al.* [13,14], they also found a critical viscosity ratio separating fingering from no fingering regimes and experimentally verified the existence of a blunt tip in the interfacial structure. Overall, the three-dimensional structure inside the gap is shown to play a crucial role in miscible fingering, particularly in setting the onset of viscous fingering or suppressing it altogether. This suggests that it may be feasible to modify miscible fingering by directly altering the interfacial structure, as demonstrated by Videbæk and Nagel [18] through enhanced diffusion. Specifically, Videbæk and Nagel experimentally showed that diffusion could round the blunt tip of the interfacial structure and create a new regime of miscible fingering, by systematically lowering the Péclet number [18].

Another potential way of altering the interfacial structures is with the use of particles, which introduces new length-scale (i.e., particle diameter) into the problem. Previous studies of viscous fingering with suspensions [19–24] demonstrated that when a suspension displaces air inside a Hele-Shaw cell, particles may accumulate on the oil-air interface and cause viscous fingering inside the suspension. Here, the particle accumulation is caused by the shear-induced migration of noncolloidal particles [25], which focus the particles near the centerline and allow them to move faster than the mixture. Hence, the hydrodynamic interactions of particles inside the thin gap yield conditions for miscible fingering, which is unobserved in pure fluids. However, exact conditions of this particle-induced miscible fingering are not currently understood [22]. Furthermore, the presence of the oil-air interface complicates the physical picture, as surface tension is shown to stabilize the suspension [24].

In this paper, we focus on the onset and characteristics of particle-induced miscible fingering with no influence of surface tension, by injecting oil into a suspension of the same oil and noncolloidal particles with diameter d. We conduct systematic experiments inside a Hele-Shaw cell to identify the onset of fingering for varying particle volume fractions, ϕ_0, and gap thicknesses, b. Note that we presently keep $b/d > 10$, so that we may treat the suspension as a continuum. The presence of suspended particles is expected to increase the effective viscosity of the defending fluid, which causes miscible fingering, and to potentially alter the three-dimensional structure inside the gap. Hence, to understand the connection between fingering and interfacial structures, we experimentally extract the interfacial shape between the invading oil and the suspension inside the thin gap and also develop a lubrication model to predict the interfacial structure. Finally, we examine the effects of decreasing b in our current experiments, to demonstrate that the wall confinement may be used to modify the observed fingering behavior.

The paper is organized as follows. Section II includes the details of the experimental set-up and procedure, followed by data processing techniques, while the theoretical model is introduced in Sec. III. Section IV details the experimental results and the comparison with theory. Then, the paper concludes with the summary and outlook for future research in Sec. V.

II. EXPERIMENTAL METHOD

We experimentally demonstrate the emergence of miscible fingering when viscous oil (fluid 1) radially displaces the mixture of the same oil and noncolloidal, quasineutrally buoyant particles (fluid 2) inside a radial Hele-Shaw cell. Here, the presence of suspended particles in fluid 2 is the only factor that gives rise to the viscosity difference between two fluids and leads to viscous

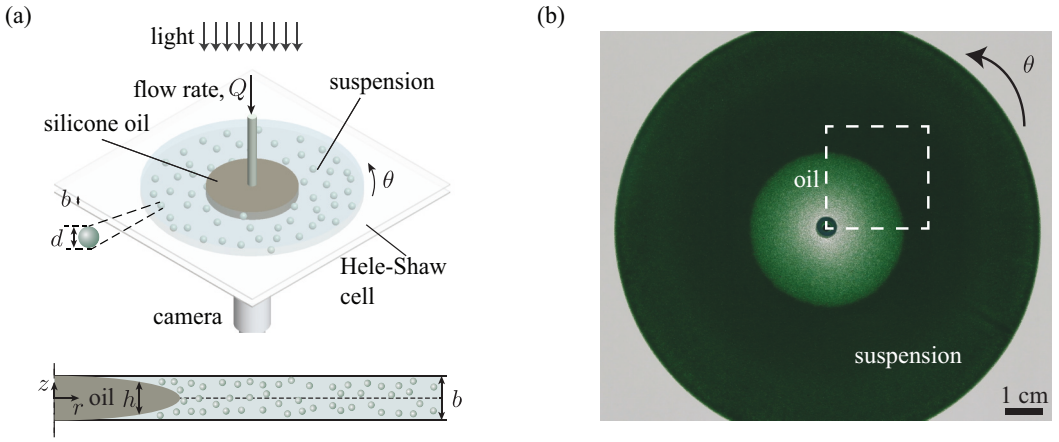

FIG. 1. (a) A schematic of the experimental setup (top). A schematic of the interfacial structure from the side view. (b) Bottom-up view of silicone oil injected into suspension of $\phi_0 = 0.25$. Here, the particle diameter $d = 100$–$150\,\mu$m, gap thickness $b = 2.31$ mm, and flow rate $Q = 9.1$ ml/min.

fingering. The radial Hele-Shaw cell consists of two square glass plates ($30 \times 30 \times 1.2$ cm) that are separated using shims (McMaster) to create a uniform gap of thickness b [Fig. 1(a)]. There is an inlet at the center of the upper plate for injecting fluids. Fluid 1 is the silicone oil with density $\rho = 0.96\,\mathrm{g/cm^3}$ and dynamic viscosity $\mu_1 = 0.096$ Pa s, while fluid 2 comprises the same silicone oil and polyethylene particles (Cospheric) with density, $\rho_p = 0.98\,\mathrm{g/cm^3}$, and diameter, $d = 100$–$150\,\mu$m. An LED panel (ASD, 2X2, 40W, 5000K) is placed parallel to the cell to provide uniform illumination of the system, and a digital camera (Nikon D500) records the evolution of clear oil invading the suspension from bottom up.

We first inject the suspension (fluid 2) into the Hele-Shaw cell via a syringe pump (Harvard). The initial concentration of suspension, ϕ_0, is varied from 0.1 to 0.35, while b is systematically varied from 1.4 to 2.31 mm in the experiments. Note that $b/d > 10$ in all the experiments so that we may regard the suspension as a continuum. During the injection of suspension, shear-induced migration [25]—particles' tendency to migrate toward the regions of low shear rate—leads to the accumulation of particles on the oil-air interface for $\phi_0 > 0.1$ [20]. When $\phi_0 \gtrsim 0.25$, the particle accumulation causes viscous fingering and the formation of dense particle clusters in the early times of injection [20,22]. Hence, to ensure a relatively uniform distribution of particles, we inject the suspension at a slow flow rate ($\sim$30 ml/min) to minimize the shear-induced migration of particles. In addition, for $\phi_0 > 0.2$, we first inject a small amount of silicone oil into the cell ahead of injecting the suspension, to reduce particle accretion. Overall, a sufficient amount of the suspension is injected inside the cell, so that the presence of the suspension-air interface does not affect the displacement of fluid 1 [see Fig. 1(b)].

We start the injection of silicone oil (fluid 1) immediately after the injection of suspension, to minimize particle settling. The volumetric flow rate, Q, of fluid 1 is chosen to ensure Q/b is constant between experimental runs with varying b (see Table I). Figure 1(b) shows a typical bottom-up image extracted from an experiment with no miscible fingering. In Sec. IV, we will only show a

TABLE I. Injection rates of silicone oil.

Gap thickness (b)	1.4 mm	1.8 mm	2.31 mm
Oil injection rate (Q)	5.5 ml/min	7.1 ml/min	9.1 ml/min

quarter of the experimental images [a dashed square in Fig. 1(b)] to more closely showcase the morphology of the interface.

In the current system, there are two types of Péclet numbers to consider. First, analogous to miscible fingering with pure fluids (e.g., Ref. [18]), the first Péclet number, Pe, corresponds to the ratio between axial advection, Ub, and and the diffusion of suspended particles, D, so that $\mathrm{Pe} = Ub/D \sim O(10^{10})$. Here, $U = Q/(2\pi Rb)$ is the characteristic speed of the oil-suspension interface, while $D = kT/(3\pi\mu_1 d) \sim 10^{-17}\,\mathrm{m}^2/\mathrm{s}$, where kT is the thermal energy of the suspending fluid. In the pure fluid counterpart, the diffusion coefficient is instead defined as the interfluid diffusivity. Second, a particle-scale Péclet number, $\mathrm{Pe}_{\dot\gamma}$, is based on the characteristic shear rate, $\dot\gamma \sim U/b$, so that $\mathrm{Pe}_{\dot\gamma} = \dot\gamma d^2/D \sim O(10^7) - O(10^8)$. Notably, $\dot\gamma d^2$ represents the scaling for shear-induced migration of particles across the streamlines [25,26]. Overall, we reasonably assume that axial advection dominates over shear-induced diffusion as well as thermal diffusion of suspended particles, as $\mathrm{Pe} \gg \mathrm{Pe}_{\dot\gamma} \gg 1$. Hence, a well-defined interface exists between the invading oil and the suspension in the current experiments.

A. Data analysis

For the experiments with pure miscible fluids at large Pe [13,17], the onset of lateral fingering instability (in the r-θ plane) is observed to coincide with the transition in the interfacial structure spanning the gap in the z direction [see the schematic in Fig. 1(a)]. In our current experiments with suspensions, we verify this connection between the lateral instability and the interfacial structure in the z direction through image processing. The lateral interfacial pattern between the pure fluid (fluid 1) and the suspension (fluid 2) in the r-θ plane can be captured from images taken from directly below the Hele-Shaw cell. However, the shape of the interface in the r-z plane is calculated based on the depth-averaged concentration of the particles, in two steps that correlate with our two-step injection process.

First, we measure the concentration profile based on the Beer-Lambert law [27]. The Beer-Lambert law relates the changes in the light intensity of the image $I(r,\theta)$ to the depth-averaged particle concentration, $\bar\phi(r,\theta) = b^{-1}\int_{-b/2}^{+b/2}\phi(r,\theta,z)dz$:

$$\log\left[I_0/I(r,\theta)\right] = k\bar\phi(r,\theta), \tag{1}$$

where I_0 is the light intensity in the reference image of an empty cell, and k is the attenuation coefficient. To obtain the value of k, we use the initial injection of the suspension for varying ϕ_0 as the calibration experiments. Then, we integrate Eq. (1) over the area occupied by the suspension, Ω, and apply mass conservation, which yields

$$k = \frac{\int_\Omega \log\left[I_0/I(r,\theta)\right]dA}{\phi_0\Omega}, \tag{2}$$

where $\phi_0\Omega b$ corresponds to the total volume of particles injected during the initial process.

Next, we extract the shape of the interface between the silicone oil and suspension in the r-z plane upon the injection of oil. We assume that oil penetrates the suspension symmetrically about the centerline ($z = 0$) to form a three-layer structure, as illustrated in Fig. 2(b). Analogous three-layer structures were previously verified in the miscible displacement of pure fluids both in experimental observations and theoretical calculations [15,17]. Based on the three-layer structure, the depth-averaged particle concentration upon oil injection must be given by

$$\bar\phi(r)b = [b - h(r)]\bar\phi_{t/b}(r), \tag{3}$$

where h is the thickness of the middle oil layer, and $\bar\phi_{t/b}(r)$ is the depth-averaged concentration of the top and bottom suspension layers. Note that $\bar\phi(r)$ can be computed by averaging Eq. (1) over θ from $-\pi$ to π, with the value of k determined in the previous step. By averaging $\bar\phi(r,\theta)$ over θ, we currently do not capture the variations in $\bar\phi$ that occur in the event of lateral miscible fingering.

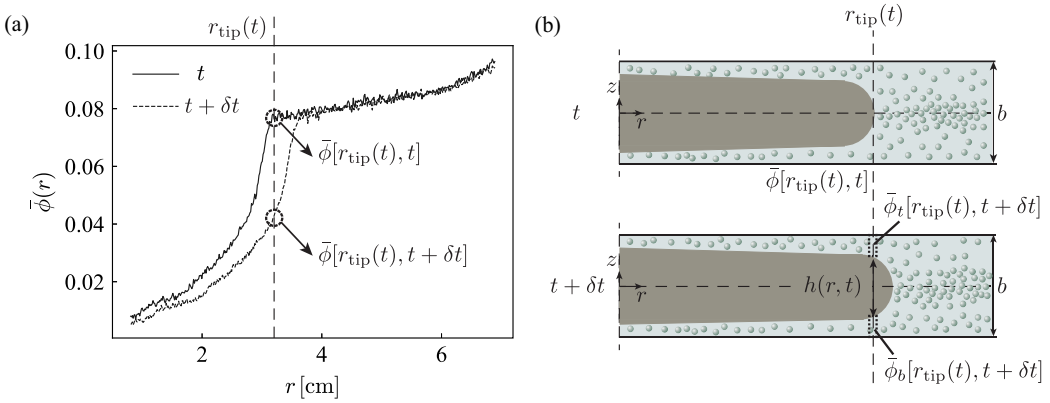

FIG. 2. (a) The depth-averaged concentrations, $\bar{\phi}(r)$, is measured at two adjacent times, t and $t+\delta t$ for $\phi_0 = 0.1$ and $b = 1.40$ mm. (b) The schematic illustrates the three-layer structure when oil penetrates the suspension in the r-z plane. $\bar{\phi}_t$ and $\bar{\phi}_b$ denote the local concentrations of suspension above and below the tip of invading oil, respectively, while h is the thickness of the middle oil layer.

Figure 2(a) shows the plot of $\bar{\phi}(r)$ for $\phi_0 = 0.1$ and $b = 1.40$ mm at two time intervals (separated by δt), and it reveals two regimes of the concentration profile. For $r < r_{\rm tip}$ where $r_{\rm tip}$ is the location of the tip of invading oil, $\bar{\phi}(r)$ is close to zero near $r = 0$ and rises steeply due to the presence of an oil layer with a decreasing thickness. For $r > r_{\rm tip}$ where oil has not yet invaded, $\bar{\phi}(r)$ increases only slightly, which points to the effects of the particle accumulation near the oil-air interface. As shown in Fig. 2(a), there is a notable drop in $\bar{\phi}[r_{\rm tip}(t), t+\delta t]$ from the previous time step (i.e., $\bar{\phi}[r_{\rm tip}(t), t]$). We hereby assume that this drop in $\bar{\phi}$ arises entirely from the presence of the oil layer, while the suspension concentration in the top and bottom layers is unaffected by oil invasion, such that $\bar{\phi}_{t/b}[r_{\rm tip}(t), t+\delta t] = \bar{\phi}[r_{\rm tip}(t), t]$ for small δt. Once $\bar{\phi}_{t/b}(r)$ is thus set as the tip sweeps across all r, we can obtain the oil thickness $h(r)$ by rearranging Eq. (3).

Notably, the assumption of a uniform particle distribution inside the gap neglects the effects of shear-induced migration that may focus particles near the centerline during initial injection. Hence, $\bar{\phi}_{t/b}(r)$ based on the uniform concentration assumption may be greater than the actual value for certain parameter regimes, thereby overestimating h, as $h(r)/b = 1 - \bar{\phi}(r)/\bar{\phi}_{t/b}(r)$. If the error in $\bar{\phi}_{t/b}(r)$ is given by $\epsilon\bar{\phi}_{t/b}(r)$, where $\epsilon < 1$, the corresponding deviation in h/b is approximately equal to $\epsilon(1 - h/b)$ based on the Taylor expansion of Eq. (3). The estimated errors in h/b will be included in Sec. IV B.

III. THEORETICAL FORMULATION

In addition to experiments, we model the radial miscible displacement of fluid 1 into fluid 2 inside a Hele-Shaw cell of height b, at a constant volumetric flow rate Q (see the schematic in Fig. 3), to predict the transition in interfacial structures. The flow is assumed to be axisymmetric; therefore, we consider the flow as being two-dimensional in the r-z plane. Note that the axisymmetric assumption strictly holds only in the flow regime where there is no lateral instability. In addition, we model fluid 1 and fluid 2 as generalized Newtonian fluids with known viscosities, μ_1 and μ_2, respectively. The density difference between the two fluids is small enough to be neglected, so we denote ρ as the density of both fluids. Consistent with the experiments, we also consider the regime of $\mathrm{Pe} \gg \mathrm{Pe}_{\dot{\gamma}} \gg 1$, so that there is no diffusive mixing between the two fluids. Thus, there exists a sharp interface at the position $z = \pm h(r,t)/2$ between fluid 1 and fluid 2. Note that this current model is a straightforward extension of the theoretical analyses by [13,15] in a radial geometry in the limit of zero buoyant forces.

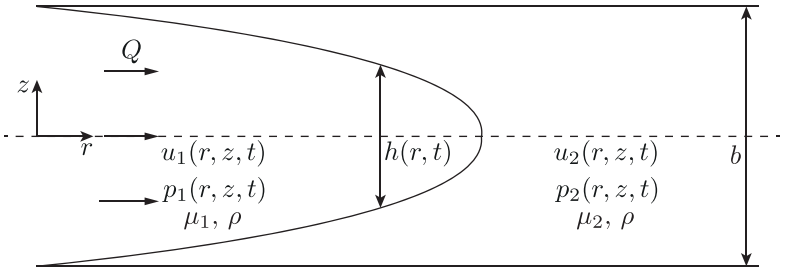

FIG. 3. Sketch of the flow system: radial miscible displacement of fluid 1 into fluid 2 with a constant flow rate Q inside a Hele-Shaw cell of gap thickness b. The two miscible fluids are separated by a sharp interface of thickness $h(r,t)$.

We briefly comment on our treatment of fluid 2 as a Newtonian fluid, although it comprises particles and fluid 1 as the suspending liquid. The Newtonian assumption is valid in the limit of $\mathrm{Pe}_{\dot\gamma}/\mathrm{Re}_{\dot\gamma} \gg 1$ [28], where $\mathrm{Re}_{\dot\gamma} = \rho d^2\dot\gamma/(4\mu_1)$ is the Reynolds number based on the shear rate. As $\mathrm{Pe}_{\dot\gamma} \sim O(10^7) - O(10^8)$ and $\mathrm{Re}_{\dot\gamma} \sim O(10^{-5})$ based on the characteristic parameters, the Newtonian fluid assumption is justified in our current experiments. We also neglect nontrivial hydrodynamic interactions of suspended particles, which may cause a nonuniform particle distribution inside the suspension (fluid 2) and particle migration into clear oil (fluid 1). While this assumption may reasonably hold for $\mathrm{Pe} \gg \mathrm{Pe}_{\dot\gamma}$, we will revisit the implication of our model assumptions when we compare our solution to the experimental results in Sec. IV B.

We hereby focus on computing the long-time evolution of interface $h(r,t)$, which is assumed to be symmetric about the centerline $z = 0$. In the limit where the interface is developed over a radial distance much larger than b, we employ lubrication approximations [29] and show that pressure p is uniform across the gap in the absence of surface tension, or $p_1 = p_2 = p(r,t)$. In addition, the momentum balance in the r-direction reduces to

$$\frac{\partial p}{\partial r} = \frac{\partial}{\partial z}\left(\mu_1 \frac{\partial u_1}{\partial z}\right), \qquad \frac{\partial p}{\partial r} = \frac{\partial}{\partial z}\left(\mu_2 \frac{\partial u_2}{\partial z}\right), \tag{4}$$

where u_1 and u_2 correspond to radial velocity components in fluid 1 and fluid 2, respectively. We solve Eq. (4), subject to no slip boundary conditions (i.e., $u_1(\pm b/2) = u_2(\pm b/2) = 0$) and the continuity of velocity and tangential stress at $z = \pm h(x,t)/2$. The resultant velocity profiles are given by

$$u_1(r,z,t) = \frac{1}{8\mu_1}\frac{\partial p}{\partial r}\left[4z^2 - \frac{b^2 + h^2(M-1)}{M}\right], \tag{5a}$$

$$u_2(r,z,t) = -\frac{1}{8\mu_1}\frac{\partial p}{\partial r}\left[\frac{b^2 - 4z^2}{M}\right], \tag{5b}$$

where $M \equiv \mu_2/\mu_1$ is the mobility ratio.

We hereby define the depth-averaged velocities of the two fluids, $\bar u_1$ and $\bar u_2$, as

$$\bar u_1(r,t) = \frac{1}{h}\int_{-h/2}^{h/2} u_1(r,z,t)dz, \qquad \bar u_2(r,t) = \frac{2}{b-h}\int_{h/2}^{b/2} u_2(r,z,t)dz. \tag{6}$$

Assuming fluids 1 and 2 are incompressible, we require that $Q = 2\pi r[h\bar u_1 + (b-h)\bar u_2]$, to satisfy mass conservation. Substituting the average velocities into the continuity equation results in the expression for the pressure gradient,

$$\frac{\partial p}{\partial r} = -\frac{6\mu_1 MQ}{\pi r[b^3 + h^3(M-1)]}. \tag{7}$$

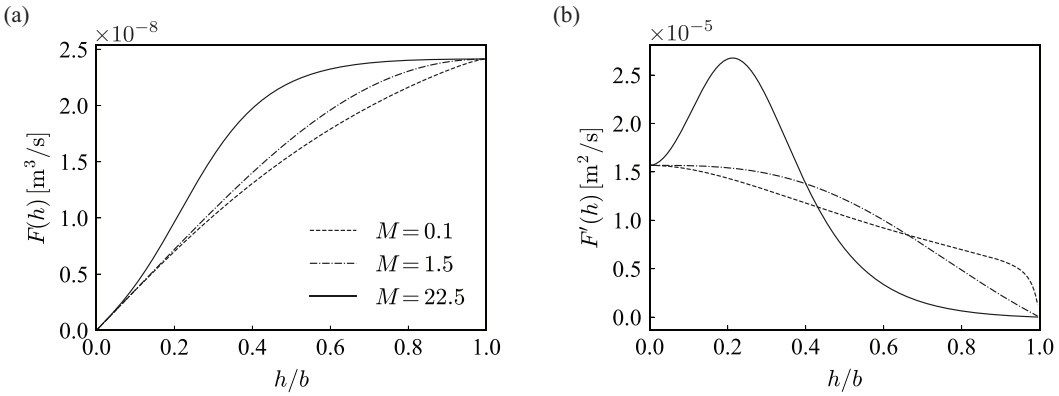

FIG. 4. (a) The plot of the flux function $F(h)$ versus h/b for the mobility ratios: $M = 0.1$, $M = 1.5$, and $M = 22.5$. (b) The characteristic speed $F'(h)$ plotted as a function of h/b for the same values of M.

Finally, the depth-averaged conservation of mass for fluid 1 corresponds to the following equation:

$$\frac{\partial h}{\partial t} + \frac{1}{r}\frac{\partial F(h)}{\partial r} = 0, \tag{8}$$

where the flux $F(h)$ is equal to

$$F(h) \equiv rh\bar{u}_1 = \frac{Qh}{4\pi}\left[\frac{3b^2 + h^2(2M-3)}{b^3 + h^3(M-1)}\right]. \tag{9}$$

Then, the characteristic speed, $F'(h)$, corresponds to

$$F'(h) = \frac{dF}{dh} = \frac{3Qb^2}{4\pi}\left\{\frac{(b-h)[b^2 + bh + 2h^2(M-1)]}{[b^3 + h^3(M-1)]^2}\right\}. \tag{10}$$

We can characterize the solutions to Eq. (8) by closely examining the flux function, $F(h)$, and the characteristic speed, $F'(h)$ [30]. As shown in Fig. 4(a), when $M \leqslant 1.5$, $F(h)$ is concave over the entire region: $0 \leqslant h/b \leqslant 1$. Accordingly, $F'(h)$ decreases monotonically for increasing h/b, as shown in Fig. 4(b). This implies that the interface near the centerline (small h near r_{tip}) travels with a faster characteristic speed than near the wall (large h near $r = 0$). Therefore, the interface profile is self-spreading, and no shocks form in this regime.

When $M > 1.5$, $F(h)$ becomes convex for small h where $F'(h)$ increases. The nonmonotonicity of $F'(h)$ implies that the interface near the wall ($r = 0$) could travel faster than near the centerline (r_{tip}). This decrease in the characteristic speed toward the tip of the profile causes the interface to steepen over time, resulting in shock fronts. Thus, $M = 1.5$ marks the occurrence of convexity in the flux function (i.e., $F''(h) = 0$) and meets the condition for shock formation. We hereby refer to $M_{\mathrm{s}} = 1.5$ as the threshold mobility ratio for shock formation, which matches the theoretical results of miscible two-fluid flows in a rectilinear Hele-Shaw cell [14,15] and a two-layer viscous gravity current [31].

To solve for $h(r,t)$, we define a similarity variable, $\xi = r/\sqrt{t}$, which reduces Eq. (8) to

$$\left(F'(h) - \frac{1}{2}\xi^2\right)\frac{dh}{d\xi} = 0. \tag{11}$$

While $dh/d\xi = 0$ is trivial, the solution to $F'(h) - \xi^2/2 = 0$ yields an expression for $h(\xi)$ that strongly depends on M. Two resultant expressions for $h(\xi)$ are shown in Fig. 5, corresponding to $M = 1.33$ (no shock) and $M = 10$ (shock). Note that, in the limit of $M < M_{\mathrm{s}} = 1.5$, $h(\xi)$ gradually decreases to zero with increasing ξ, which corresponds to a self-spreading profile. However, for

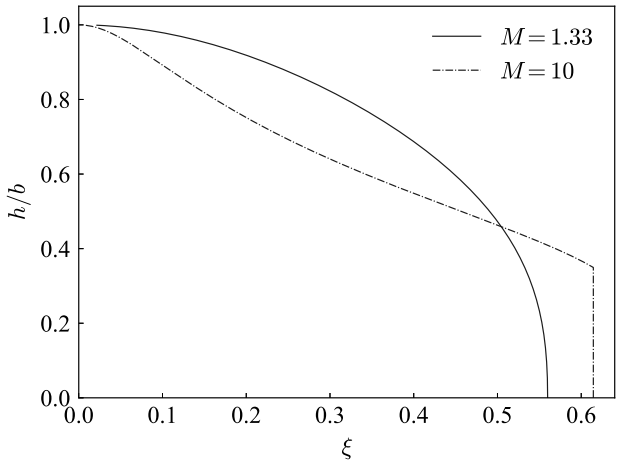

FIG. 5. The plot of similarity solutions, $h(\xi)$, for $M = 1.33$ (solid line) and $M = 10$ (dashed line).

$M > M_s = 1.5$, the expression for $h(\xi)$ becomes multi-valued and does not satisfy the entropy condition. Hence, in this regime, we employ an "equal-area" rule as well as the Oleinik entropy condition [30,31], to compute the position of the shock, ξ^*. We subsequently construct a composite solution of $h(\xi)$ that comprises a shock front at ξ^* and the solution to $F'(h) - \xi^2/2 = 0$ for $0 \leqslant \xi < \xi^*$. Hence, the plot of $h(\xi)$ for $M = 10$ in Fig. 5 features a smooth profile of decreasing thickness that sharply transitions to a vertical shock front at $\xi^* = 0.615$.

IV. RESULTS

A. Onset of (lateral) miscible fingering

We first experimentally demonstrate the emergence of the lateral fingering patterns in the r-θ plane, as the initial concentration ϕ_0 of suspension and gap thickness b of the Hele-Shaw cell are varied. Figure 6(a) shows the top-right quarter of the experimental images that were taken 105 s after the injection of silicone oil. For every experiment, the value of ϕ_0 sets the mobility ratio between the outer and inner fluids, $M = \mu_2/\mu_1$, based on the following constitutive law [32]:

$$\frac{\mu_2}{\mu_1} = 1 + 2.5\frac{\phi_0}{1-\phi_0/\phi_m} + \mu^c(\phi_0)\frac{\phi_0/\phi_m}{1-\phi_0/\phi_m}, \tag{12}$$

where $\mu^c = \mu_{01} + (\mu_{02} - \mu_{01})/[1 + I_0\phi_0^2(\phi_m - \phi_0)^{-2}]$, $\phi_m = 0.585$, $\mu_{01} = 0.32$, $\mu_{02} = 0.7$, and $I_0 = 0.005$. Over the range of ϕ_0 tested (i.e., 0.1–0.35), M is varied from 1.33 to 4.72, while $b/d > 10$ for all the experiments.

The experimental images in Fig. 6(a) reveal three notable observations about the lateral patterns in the bottom-up view. First, while there is no true interface between the clear oil (fluid 1) and the mixture of particles and the same oil (fluid 2), the location of the tip of invading oil, r_{tip}, is clearly observable from the bottom-up view. The tip separates the relatively clear region with a varying suspension concentration from the region of a uniform concentration. Hence, we refer to this tip location as the "interface" between fluid 1 and fluid 2. Second, when $M < 2$, this interface remains relatively circular for the entire duration of the oil injection, for all values of b/d. Finally, a further increase in M triggers the interfacial deformations in the r-θ plane.

To quantify the onset of fingering, we systematically detect the shape of the interface (in the r-θ plane) at the end of every experiment and calculate the magnitude of the averaged interfacial deformations, $\bar{l}$, as shown in the image of Fig. 6(b). We plot $\bar{l}$ as a function of M in Fig. 6(b) and reveal that the deformations are statistically the same for $M < 3$ and undergo a sharp increase when

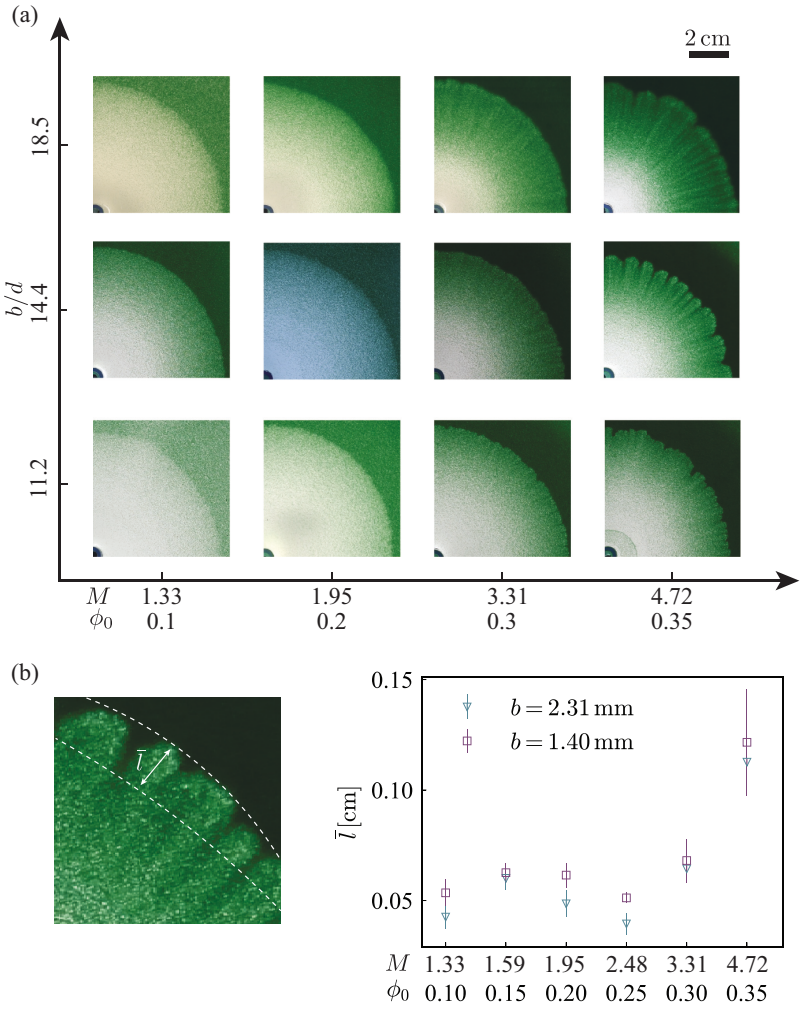

FIG. 6. (a) State diagram: quarter images of experiments with varying ϕ_0 and b/d. Images were taken after 105 s of the injection of pure oil. (b) The schematic illustrates the averaged interfacial deformation $\bar{l}$ (left panel), which is plotted as a function of M on the right-side panel for $b = 1.40$ mm and 2.31 mm.

$M > 3$ for $b = 2.31$ mm and 1.40 mm. Based on this transition in $\bar{l}$, we currently note $M_{\rm cr} \approx 3$ as the critical mobility ratio at which miscible fingering commences. The critical viscosity ratio $M_{\rm cr}$ appears to be independent of b/d, for the range of b/d values tested. Furthermore, it matches the onset observed by Bischofberger *et al.* [17] for miscible fingering of pure liquids. However, $M_{\rm cr} \approx 3$ is distinctly larger than the theoretical prediction of $M_{\rm s} = 1.5$ at which shock fronts form, which will be discussed in the next section.

B. Interfacial structures: Comparison with theory

As previously demonstrated in [13,17], the emergence of lateral fingering in the r-θ plane is closely correlated to interfacial structures (i.e., $z = \pm h(r, t)/2$) spanning the gap in the r-z plane. To examine this connection between interfacial structures and the associated changes in lateral patterns, we extract the interfacial structures for varying M from the experiments, and compare them with our theoretical results developed in Sec. III.

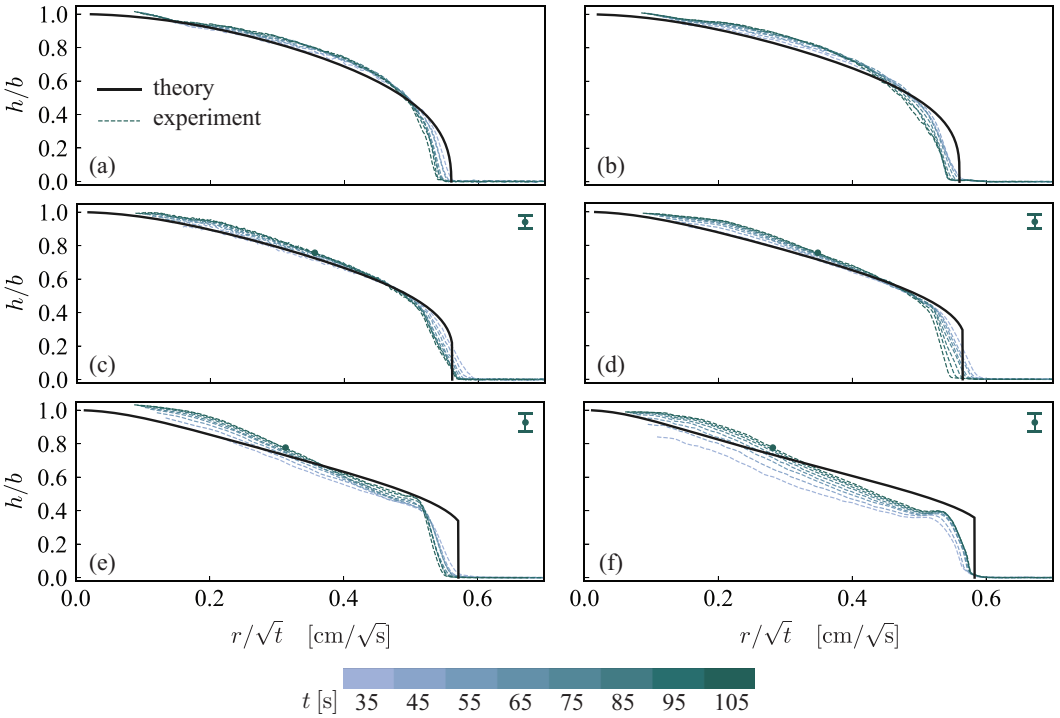

FIG. 7. (a)–(f) Interfacial structures of experiments (dashed lines) with $b = 2.31$ mm and mobility ratios: $M = 1.33, 1.59, 1.95, 2.48, 3.31, 4.72$. The profiles of light to dark colors correspond to different instants in time from 35 to 105 s (increment of 10 s) in the experiment (see the color bar for the reference). The error bars shown in panels (c)–(f) correspond to the estimated error in h/b associated with the uniform concentration assumption at $h/b = 0.75$ and $t = 105$ s, which is denoted with a solid dot on the interfacial shape. The solid lines correspond to the theoretical results for the same values of M.

Figures 7 and 8 show the plots of the thickness of the invading oil $h(r, t)$, normalized by the gap thickness b, with mobility ratios $M = 1.33$–4.72, at $b = 2.31$ and 1.40 mm, respectively. The dashed curves denote the experimental results between 35–105 s, following the injection of pure oil at every 10 s interval. The horizontal axis is the radial distance from the inlet scaled by the square root of the corresponding time of injection, or $\xi = r/\sqrt{t}$. The solid lines correspond to the theoretical predictions of $h(\xi)$ for the same values of M from Sec. III. The experimental plots of $h(r, t)$ in Figs. 7 and 8 show that blunt tips start to form for $1.5 < M < 3$, consistent with the theoretical prediction, while lateral fingering is observed experimentally for $M > 3$. This apparent discrepancy between $M_{cr} = 3$ from the experiments and $M_s = 1.5$ from theory implies that the shock formation in the r-z plane is not a sufficient condition for lateral miscible fingering in the r-θ plane. Alternatively, the invading oil may eventually become unstable at $M \geqslant 1.5$ if given more time, and the timescale set by our current Hele-Shaw cell is unable to capture the eventual onset of fingering.

Overall, the experimental interfacial structures in Fig. 7 collapse onto a single curve when plotted as a function of the similarity variable $\xi = r/\sqrt{t}$, which supports the existence of similarity solutions in Sec. III. Specifically, for $M = 1.33$ and 1.59 [Figs. 7(a) and 7(b)], the interfacial shapes appear smooth throughout and gradually decrease from $h/b = 1$ to 0 with increasing ξ. As M is further increased [Figs. 7(c) and 7(d)], the interfacial structures from the experiments distinctly develop blunt tips (near $\xi \sim 0.6$) that gradually connects to $h/b = 1$ as $\xi \to 0$. Finally, for $M = 3.31$ and 4.72, the blunt tips at the nose of the invading oil become even more pronounced with a visible "bump" that lengthens with M, as shown in Figs. 7(e) and 7(f). For $M \geqslant 1.95$ (or

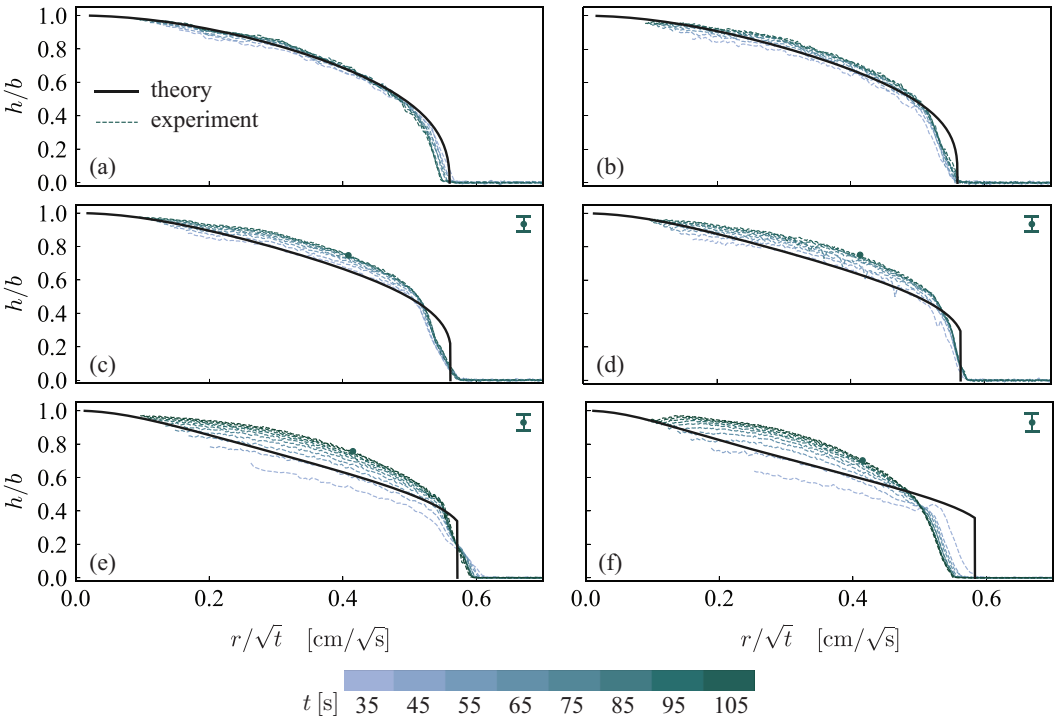

FIG. 8. Interfacial structures of experiments (dashed lines) with $b = 1.4$ mm and mobility ratios: $M =$ 1.33, 1.59, 1.95, 2.48, 3.31, 4.72. The light to dark colors correspond to increasing times from 35 s to 105 s (in the increment of 10 s) in the experiment. The error bars shown in panels (c)–(f) are the estimated errors in h/b associated with the uniform concentration assumption at $h/b = 0.75$ and $t = 105$ s, denoted with a solid dot on the interfacial shape. The solid lines correspond to the theoretical results for the same values of M.

$\phi_0 \geqslant 0.20$), we anticipate that the particles in the outer fluid are not uniformly distributed due to shear-induced migration during the initial injection. Hence, we have included the approximate size of the overestimation in h/b [i.e., $\epsilon(1 - h/b)$] as error bars in Figs. 7(e) and 7(f). We estimate the deviation in $\bar{\phi}_{t/b}(r)$, or $\epsilon\bar{\phi}_{t/b}(r)$, based on the measurements of the steady-state particle distribution inside the pressure-driven tube flow in Ref. [33].

As shown in Figs. 7(a)–7(d), the match between experiments and similarity solutions for $M =$ 1.33–2.48 is reasonable in the region away from the tip, where the lubrication approximations are valid. In addition, the theoretical results predict the development of a blunt tip for $M > 1.5$, which grows in thickness with a further increase in M, in qualitative agreement with the experiments. However, the current theoretical model fails to correctly predict the shape of the tips, as the lubrication model is expected to break down in nearly vertical shock fronts. For $M = 3.31$ and 4.72 [Figs. 7(e) and 7(f)], the theoretical results deviate significantly from the experiments, both near and even away from the tip. These notable deviations between theory and experiments in Figs. 7(e) and 7(f) can be further attributed to the fact that lateral fingering has commenced experimentally in the r-θ plane, while our 2D model is strictly valid in the stable, axisymmetric base flow.

Figure 8 shows the interfacial structures for experiments with mobility ratios $M = 1.33$–4.72 at the smallest gap thickness, $b = 1.40$ mm. Consistent with the case of $b = 2.31$ mm, the interfacial shapes in Fig. 8 develop blunt fronts for $M > 1.5$, which qualitatively matches our theoretical findings. For $M = 1.33$–2.48 with no miscible fingering, the experimental interfacial structures appear to be self-similar when plotted as a function of $\xi = r/\sqrt{t}$ [see Figs. 8(a)–8(d)]. However, the self-similar evolution of the interfacial shapes breaks down for $M > 3$, and their shapes are

notably different from those at $b = 2.31$ mm which exhibit a bump near the tip. The changes in the interfacial shapes for varying b/d will be further discussed in Sec. IV C.

For the experiments at $b = 1.40$ mm, the comparison with the theoretical model varies greatly with the values of M. Note that our theoretical model is independent of the gap thickness, since the existence of particles is assumed to alter the bulk viscosity of the outer fluid only. In the dilute regime (i.e., $M = 1.33, 1.59$) where the interfaces are relatively smooth, our theoretical model is able to closely predict the experimental interfacial structures, especially in the region away from the tip. In addition, the theoretical model is effective in predicting the existence of the blunt tip for $M > 1.5$. However, distinct from the experiments at $b = 2.31$ mm, the model is no longer able to correctly predict the shape of the interface away from the tip even for moderate mobility ratios (i.e., $M = 1.95, 2.48$). For $M = 1.95$–4.72, the deviation between experiments and theory away from the tip may be partly explained by the overestimation in h/b stemming from the uniform concentration assumption [see the error bars in Figs. 8(c)–8(f)]. Furthermore, for $M > 3$ in which lateral fingering occurs, the deviations between theory and experiments become even more significant. Overall, as b is reduced, the continuum model may become invalid especially in the thin film region near the wall.

For all the data presented in Figs. 7 and 8, the blunt tips in the experimental interfacial structures ($M > 1.5$) are notably less steep than those of the liquid counterpart reported in Refs. [13,14,17]. To understand this, we must consider inherent uncertainties in our measurements of h that may contribute to this observation. For $M > 3$ where there is lateral fingering, the azimuthal variations in $\bar{\phi}$ and h are expected, which we currently neglect by averaging $\bar{\phi}(r, \theta)$ from $\theta = -\pi$ to π. As shown in Fig. 12 in the Appendix, the plots of $h(r, \theta)$ at the "peak" versus "valley" of the finger reveal clear deviations near the tip of invading oil. More importantly, they showcase distinctly more steep fronts than the θ-averaged profile (shown in solid line). Hence, averaging our experimental data over θ at least partly contributes to why our experimental h is distinctly less blunt than the pure liquid cases. The size of this error is expected to scale as the characteristic finger length, $\bar{l} \sim 0.1$ cm for $M > 3$, as plotted in Fig. 6(b).

In addition to errors in data extraction, the key difference between our current study and miscible displacements of pure fluids lies in the range of relevant Péclet numbers. In the study of pure liquids [13,14,17], the Péclet number is defined as $\mathrm{Pe}_f = Ub/D_f$, where D_f refers to the diffusivity that promotes interfluid mixing, distinct from particle diffusivity, D. Particularly, blunt tips in h are observed for $\mathrm{Pe}_f > 10^4$ [13,14,17,18] and become rounded as Pe_f is lowered below 10^3 [18]. This is also consistent with the numerical simulations of Chen *et al.* [34] who showed the existence of a steep front only for $\mathrm{Pe}_f > 800$. In the current study with suspensions, we have two distinct Péclet numbers—$\mathrm{Pe} = Ub/D \sim O(10^{10})$ and $\mathrm{Pe}_{\dot{\gamma}} = \dot{\gamma} d^2/D \sim O(10^7) - O(10^8)$. Then, the most relevant dimensionless parameter that governs the shape of the blunt tip is the ratio between axial advection and shear-induced diffusion, or $\lambda = \mathrm{Pe}/\mathrm{Pe}_{\dot{\gamma}} = (b/d)^2$, which is in the order of 10^2. Therefore, in the current range of $\lambda < 10^3$, the interfacial structures are expected to be less steep than those in [13,14,17]. We will more closely consider the effects of systematically reducing b/d and, henceforth, λ in Sec. IV C.

C. Effects of decreasing b/d

As we demonstrated in the previous section, the decrease of gap thickness can alter the interfacial structures, while it does not affect the onset of lateral miscible fingering. In this section, we focus on the changes in the morphologies of miscible fingering that accompany the changes in interfacial structures, as b is decreased.

We first revisit the evolution of $h(r, t)$ extracted from experiments with no miscible fingering ($M = 1.33$) in Fig. 9(a). The solid lines represent the experiment with the largest gap ($b = 2.31$ mm) from $t = 15$ s to $t = 105$ s, while the dashed lines correspond to the experiment with the smallest gap ($b = 1.4$ mm). The plots of $h(r, t)$ demonstrate that the interfacial shapes in the stable regime are largely independent of b/d. Figure 9(b) also shows the bottom-up images from the experiments

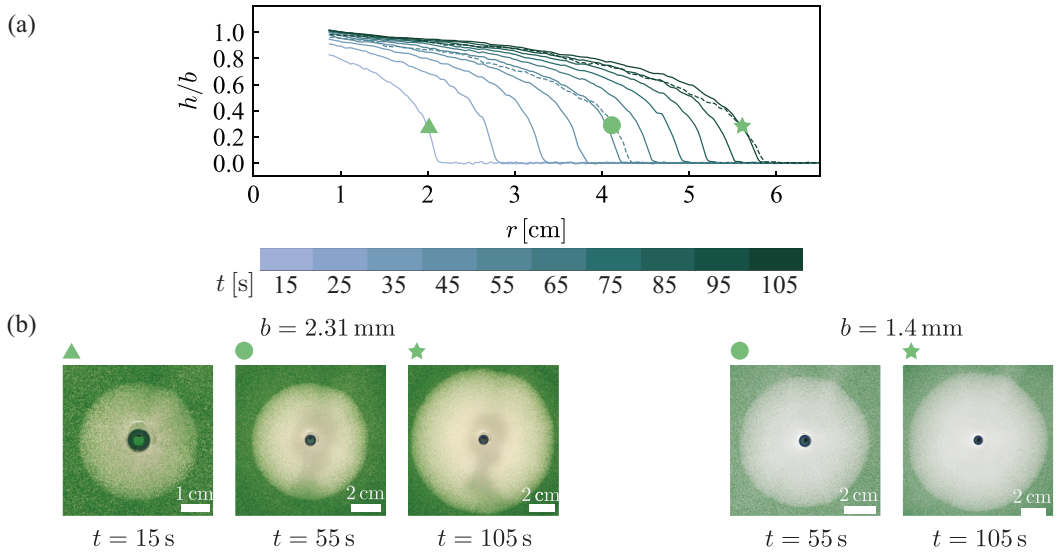

FIG. 9. (a) At $M = 1.33$, interfacial structures feature a parabolic shape and are largely independent of the gap thickness: $b = 2.31$ mm (solid lines) and 1.4 mm (dashed lines). The profiles of light to dark colors correspond to different times from 15 s to 105 s (every 10 s) in the experiment. (b) Bottom-up images from the experiments show that there is no miscible fingering.

at three specific times, which are denoted with a triangle, a circle, and a star. They confirm that there are indeed no lateral deformations of the interface in this regime.

Based on the results presented in Figs. 7 and 8, we expect notable changes in interfacial structures at large M. Hence, we focus on the experiments corresponding to $M = 4.72$ and systematically decrease b. Figure 10(a) shows the development of interfacial structures for $b = 2.31$ mm and $M = 4.72$, which are accompanied by the images of lateral patterns in the r-θ plane at three separate times. Although a blunt tip exists in the r-z plane immediately following the injection of oil, the magnitude of lateral interfacial deformations is not pronounced at early times. The lateral deformations are observed to grow with time, as the blunt tip invades the suspension and creates a plateau of thickness $h/b \approx 0.4$.

In addition, the zoomed-in image in Fig. 10(b) shows there are slender, localized regions of high particle concentration that appear at the center of a finger and do not reach the interface or the tip of the invading oil. We refer to these regions as stripes, and they result from the inner-splitting phenomenon predicted by Oliveira and Meiburg with their 3D numerical simulations [16] and experimentally verified by Bunton *et al.* [35] through Schlieren imaging. Specifically, the stripes stem from the stream-wise vorticity component that spans the gap thickness across fluids 1 and 2, which cannot be predicted by the traditional depth-averaged (Darcy) model. This secondary flow convects particles near the walls to the center of fluid 1 inside the gap.

Figures 10(c)–10(f) show the development of interfacial structures and corresponding lateral patterns for experiments at $M = 4.72$, for $b = 1.8$ mm and $b = 1.4$ mm, respectively. For both cases, lateral patterns denoted with a triangle show that miscible fingering is initiated with a blunt tip in the r-z plane. However, while the lateral deformations continue to grow in time, the blunt tip becomes rounded at a rate that is inversely proportional to the value of b/d. Furthermore, stripes are no longer observed inside individual fingers, as shown in Figs. 10(d) and 10(f). This suggests that reducing b/d helps suppress the effects of streamwise vorticity that generate stripes, which is currently not well understood.

We presently focus on the gradual rounding of the blunt tip, as observed in Figs. 10(c) and 10(e). We define the total time it takes for the blunted tips to "disappear" as t_r and systematically measure

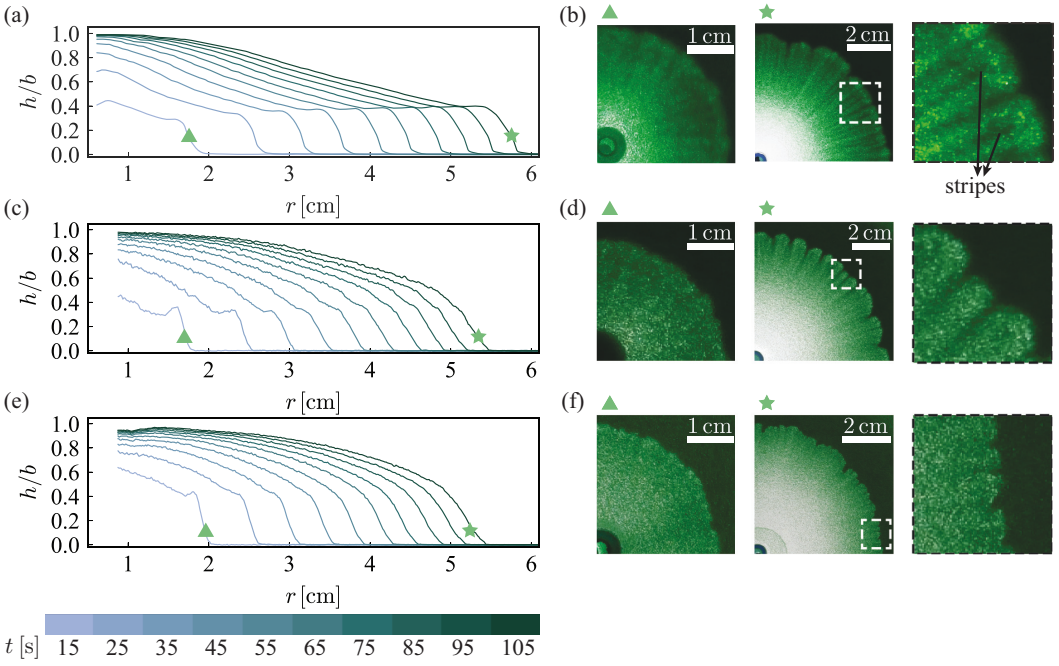

FIG. 10. Interfacial structures from experiments with $\phi_0 = 0.35$ are shown in panels (a), (c), and (e), at three gap thicknesses, $b = 2.31,\ 1.8,\ 1.4$ mm, respectively. The profiles of light to dark colors correspond to different instants in time from 15 to 105 s (every 10 s) in the experiment. The corresponding bottom-up images (denoted by a triangle and a star) and a zoomed-in image show the details of the interface. In particular, the zoomed-in images in panels (b), (d), and (f) show the disappearance of stripes as the gap is lowered.

it for varying b/d and two different particle diameters: $d = 125\,\mu$m and $325\,\mu$m. To quantify this behavior over a wider parameter range, we have conducted additional experiments, some of which fall in the range of $b/d < 10$. As plotted in Fig. 11, t_r appears to increase linearly with $(b/d)^2$, while it is largely independent of d.

This result can be rationalized in terms of shear-induced migration that allows the particles to diffuse irreversibly in the z direction from regions of high to low shear stress, for $\phi_0 \geqslant 0.2$ [25,33].

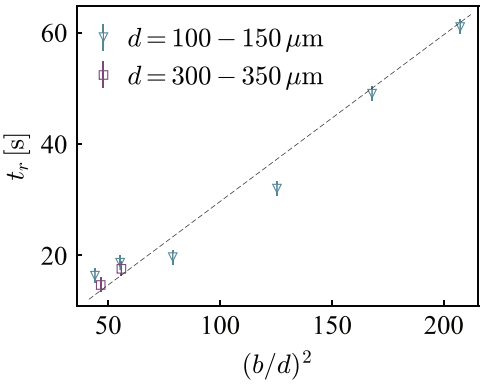

FIG. 11. The plot of t_r over $(b/d)^2$ shows an approximately linear relationship, for two particle diameters: $d = 125\,\mu$m and $325\,\mu$m.

The timescale of shear-induced migration is shown to scale as $(b/d)^2$ [23,33], or the inverse of shear-induced diffusion, $\dot{\gamma} d^2$. Therefore, the linear dependence of t_r on $(b/d)^2$ is consistent with the scaling of shear-induced migration. In particular, the projected value of t_r at $b/d = 18.5$ is 115 s, which falls outside the timescale of the experiment. Hence, this explains why the blunt tip persists for $d = 125\,\mu$m and $b = 2.31$ mm, as shown in Fig. 10(a). Furthermore, when b/d is held fixed, increasing d from 125 to 325 μm appears to have a negligible impact on t_r, which suggests that particle diffusion, $D \sim 1/d$, is not the driving mechanism behind the disappearance of blunt tips.

The decrease in b/d alters the blunt tip structure in a similar way that diffusion between two miscible fluids affects fingering in pure fluids [18]. Videbæk and Nagel experimentally discovered changes in the interfacial structures and the transition in the onset of miscible fingering when they systematically decreased the Péclet number, $\mathrm{Pe}_f = Ub/D_f$. In their study, Pe_f was varied primarily by changing the axial velocity over a wide range. In the current system with noncolloidal particles, shear-induced diffusion that scales with U is shown to drive mixing between inner and outer fluids. Hence, in lieu of varying U, we can modulate the relative importance of advection versus shear-induced diffusion by changing geometrical parameters alone (i.e., b/d), as $\lambda = \mathrm{Pe}/\mathrm{Pe}_{\dot{\gamma}} = (b/d)^2$. This potentially allows us to test the effects of enhanced diffusion on miscible fingering even at high flow rates, by changing the particle diameter at a given gap thickness. In addition, in the current range of b/d, the onset of miscible fingering itself is not affected by diffusion-induced changes in the interfacial structures. However, our preliminary experiments at $b/d < 5$ show very different behaviors of miscible fingering from the current continuum limit. Therefore, we will explore a wider range of b/d and the resultant changes in the onset and evolution of miscible fingering in the future study.

V. SUMMARY AND CONCLUSIONS

In this paper, we experimentally investigate the emergence of miscible fingering when pure oil is injected radially into a suspension made of the same oil and noncolloidal particles inside a Hele-Shaw cell. Termed particle-induced miscible fingering, this instability is caused by the presence of suspended particles in the outer fluid that sets the destabilizing mobility ratio $M > 1$. We conduct systematic experiments by varying the particle volume fraction ϕ_0 and the channel gap thickness b relative to the particle diameter d. Analogous to miscible fingering in pure fluids at large Pe [13,14,17,18], we find that miscible fingering is suppressed for small M (or small ϕ_0) and is observed with an increase in M, independent of $b/d > 10$. We experimentally characterize the critical mobility ratio to be $M_{\mathrm{cr}} = 3$, by measuring the interfacial deformations between the pure oil and the suspension in the r-θ plane, which describe the global feature of the lateral patterns.

Previous studies [13,14,17,18] have demonstrated that the onset of lateral miscible fingering is connected to the transition in the interfacial structures spanning the thin gap. To verify this connection in the present study, we experimentally extract the shape of the interface (i.e., $z = h(r,t)/2$) in the r-z plane through image processing. In addition to experimental measurements, we develop a 2D lubrication model of oil invading the suspension, assuming an asymmetric flow. We presently neglect the particle dynamics in the suspension and model the outer fluid as a simple Newtonian fluid with an increased viscosity. Hence, the model assumes that the suspended particles in the outer fluid only affect the bulk mobility ratio.

The success and limitations of the 2D model are revealed when we compare the theoretical interfacial structures with the experimental ones. The theoretical model yields interfacial structures, h, as a function of the similarity variable, $\xi = r/\sqrt{t}$, that are self-spreading at small M and form shocks at $M_{\mathrm{s}} = 1.5$. The tip region of the interfacial structure becomes blunter when $M > M_{\mathrm{s}}$. Overall, the theoretical interfacial profiles show a good quantitative match with the experiments in the region away from the tip, for small M. The deviations from the experiments become more notable for $M > 3$, which corresponds to the unstable regime with lateral miscible fingering. Furthermore, the shock formation does not coincide with the onset of miscible fingering (i.e.,

$M_s < M_{cr}$). This mismatch between theory and experiments requires additional experiments in the region of $M_s < M < M_{cr}$, to gain further physical insights into the connection between lateral patterns and interfacial structures.

Finally, we observe that the interfacial shapes are independent of b/d for small M where there is no lateral fingering. However, for $M > 3$, there are distinct changes in the interfacial structures and the resultant lateral patterns, as b is systematically reduced. Specifically, at $b/d = 11.2$ and 14.4, the blunt tips form at early times of the experiments and disappear over time; no rounding of blunt tips is observed at $b/d = 18.5$. The disappearance of the shock front happens faster with smaller b/d, which is consistent with timescale of shear-induced migration that scales with $(b/d)^2$ [23,33]. In addition, stripes, or regions of high particle concentration at the center of a finger, are observed for $M > 3$ at $b/d = 18.5$, but not at $b/d = 11.2$ and 14.4. Hence, the disappearance of blunt tips due to shear-induced migration appears to coincide with the suppression of stripes inside the fingers. All these results reveal the importance of particle dynamics in affecting the three-dimensional structure of the instability.

The results of our present study demonstrate that miscible fingering in suspensions shares many similarities with that in pure liquids (i.e., onset of fingering). Yet, there are features that are unique to suspensions and lend themselves to future studies, as the presence of suspended particles presents a new length-scale in the problem—namely, the particle diameter d. For instance, the results of decreasing b/d suggest that we may alter flow instabilities by changing the geometrical aspect ratio. Hence, we are currently exploring how the lateral patterns may evolve in the limit of $b \to d$. At the same time, stripe formation demonstrates that the three-dimensional structure (vorticity) may be used as a new tool to control transport of the outer fluid and suspended particles. Overall, the intersection of noncolloidal suspensions and classic viscous fingering features two promising research directions that are yet to be explored—modifying particle behaviors through the hydrodynamic instability, and controlling hydrodynamic instability as the particle dynamics become important.

ACKNOWLEDGMENTS

We acknowledge Dr. Li Wang for useful discussions and Mr. Zak Kujala for his help in editing the manuscript. This work was partially sponsored by the National Science Foundation through the University of Minnesota MRSEC under Award No. DMR-2011401.

APPENDIX

The interfacial structures presented in the main body of the manuscript (Figs. 7–10) have been averaged over θ from $\theta = -\pi$ to π. Hence, variations in $\bar{\phi}$ and h due to miscible fingering are currently not captured in our data. Figure 12(a) comprises plots of $h(r, t)$ at two different values of θ corresponding to the "peak" and "valley" of the finger. Compared to the average profile (shown

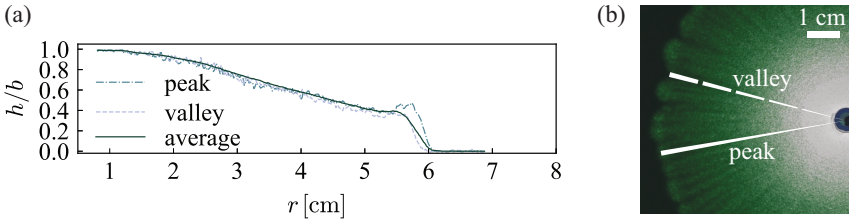

FIG. 12. (a) Interfacial structures at $t = 105$ s at θ that corresponds to a peak and a valley of a finger, as well as the θ-averaged value (solid line), for the initial concentration $\phi_0 = 0.35$ and gap thickness $b = 2.31$ mm. (b) A schematic shows the positions of the two 3° slices corresponding to the peak and the valley of a finger.

as a solid line), the profiles at distinct locations of the finger are shown to have blunter fronts. In particular, the plot of h at the peak of the finger shows a "bump" near the front that is not observed in the other profiles.

[1] P. Saffman and G. Taylor, The penetration of a fluid into a porous medium or Hele-Shaw cell containing a more viscous liquid, Proc. R. Soc. Lond. **245**, 312 (1958).

[2] G. M. Homsy, Viscous fingering in porous media, Annu. Rev. Fluid Mech. **19**, 271 (1987).

[3] F. M. Orr and J. J. Taber, Use of carbon dioxide in enhanced oil recovery, Science **224**, 563 (1984).

[4] C.-W. Park and G. M. Homsy, Two-phase displacement in Hele-Shaw cells: Theory, J. Fluid Mech. **139**, 291 (1984).

[5] E. Meiburg and G. M. Homsy, Nonlinear unstable viscous fingers in Hele-Shaw flows. II. Numerical simulation, Phys. Fluids **31**, 429 (1988).

[6] S. D. Howison, Fingering in Hele-Shaw cells, J. Fluid Mech. **167**, 439 (1986).

[7] D. A. Kessler, J. Koplik, and H. Levine, Pattern selection in fingered growth phenomena, Adv. Phys. **37**, 255 (1988).

[8] L. Paterson, Radial fingering in a Hele-Shaw cell, J. Fluid Mech. **113**, 513 (1981).

[9] R. A. Wooding, Growth of fingers at an unstable diffusing interface in a porous medium or Hele-Shaw cell, J. Fluid Mech. **39**, 477 (1969).

[10] L. Paterson, Fingering with miscible fluids in a Hele-Shaw cell, Phys. Fluids **28**, 26 (1985).

[11] H. Kim, T. Funada, D. D. Joseph, and G. M. Homsy, Viscous potential flow analysis of radial fingering in a Hele-Shaw cell, Phys. Fluids **21**, 074106 (2009).

[12] M. Nagel and F. Gallaire, A new prediction of wavelength selection in radial viscous fingering involving normal and tangential stresses, Phys. Fluids **25**, 124107 (2013).

[13] E. Lajeunesse, J. Martin, N. Rakotomalala, and D. Salin, Three-Dimensional Instability of Miscible Displacements in a Hele-Shaw Cell, Phys. Rev. Lett. **79**, 5254 (1997).

[14] E. Lajeunesse, J. Martin, N. Rakotomalala, D. Salin, and Y. C. Yortsos, Miscible displacement in a Hele-Shaw cell at high rates, J. Fluid Mech. **398**, 299 (1999).

[15] Z. Yang and Y. C. Yortsos, Asymptotic solutions of miscible displacements in geometries of large aspect ratio, Phys. Fluids **9**, 286 (1997).

[16] R. M. Oliveira and E. Meiburg, Miscible displacements in Hele-Shaw cells: Three-dimensional Navier-Stokes simulations, J. Fluid Mech. **687**, 431 (2011).

[17] I. Bischofberger, R. Ramachandran, and S. R. Nagel, Fingering versus stability in the limit of zero interfacial tension, Nat. Commun. **5**, 5265 (2014).

[18] T. E. Videbæk and S. R. Nagel, Diffusion-driven transition between two regimes of viscous fingering, Phys. Rev. Fluids **4**, 033902 (2019).

[19] H. Tang, W. Grivas, D. Homentcovschi, J. Geer, and T. Singler, Stability Considerations Associated with the Meniscoid Particle Band at Advancing Interfaces in Hele-Shaw Suspension Flows, Phys. Rev. Lett. **85**, 2112 (2000).

[20] F. Xu, J. Kim, and S. Lee, Particle-induced viscous fingering, J. Non-Newtonian Fluid Mech. **238**, 92 (2016).

[21] J. Kim, F. Xu, and S. Lee, Formation and Destabilization of the Particle Band on the Fluid-Fluid Interface, Phys. Rev. Lett. **118**, 074501 (2017).

[22] R. Luo, Y. Chen, and S. Lee, Particle-induced viscous fingering: Review and outlook, Phys. Rev. Fluids **3**, 110502 (2018).

[23] F. Xu and S. Lee, The enhancement of viscous fingering with bidisperse particle suspension, J. Fluid Mech. **860**, 487 (2019).

[24] A. Hooshanginejad, B. C. Druecke, and S. Lee, Stability analysis of a particle band on the fluid-fluid interface, J. Fluid Mech. **869**, R2 (2019).

[25] D. Leighton and A. Acrivos, The shear-induced migration of particles in concentrated suspensions, J. Fluid Mech. **181**, 415 (1987).
[26] E. C. Eckstein, D. G. Bailey, and A. H. Shapiro, Self-diffusion of particles in shear flow of a suspension, J. Fluid Mech. **79**, 191 (1977).
[27] D. F. Swinehart, The beer-lambert law, J. Chem. Educ. **39**, 333 (1962).
[28] J. J. Stickel and R. L. Powell, Fluid mechanics and rheology of dense suspensions, Annu. Rev. Fluid Mech. **37**, 129 (2005).
[29] H. Ockendon, *Viscous Flow* (Cambridge University Press, Cambridge, 1995).
[30] R. LeVeque, *Finite Volume Methods for Hyperbolic Problems* (Cambridge University Press, Cambridge, 2002).
[31] T.-F. Dauck, F. Box, L. Gell, J. A. Neufeld, and J. R. Lister, Shock formation in two-layer equal-density viscous gravity currents, J. Fluid Mech. **863**, 730 (2019).
[32] F. Boyer, É. Guazzelli, and O. Pouliquen, Unifying Suspension and Granular Rheology, Phys. Rev. Lett. **107**, 188301 (2011).
[33] B. Snook, J. E. Butler, and É. Guazzelli, Dynamics of shear-induced migration of spherical particles in oscillatory pipe flow, J. Fluid Mech. **786**, 128 (2016).
[34] C.-Y. Chen and E. Meiburg, Miscible displacements in capillary tubes: Influence of Korteweg stresses and divergence effects, Phys. Fluids **14**, 2052 (2002).
[35] P. Bunton, D. Marin, S. Stewart, E. Meiburg, and A. De Wit, Schlieren imaging of viscous fingering in a horizontal Hele-Shaw cell, Exp. Fluids **57**, 28 (2016).